Science Arts & Métiers (SAM)

is an open access repository that collects the work of Arts et Métiers Institute of Technology researchers and makes it freely available over the web where possible.

To cite this version :

Stress-strain response and volume change of a highly filled rubbery composite: experimental measurements and numerical simulations

Pierre Gilormini[a,*], Paul-Aymé Toulemonde[a,b], Julie Diani[c], Antoine Gardere[a]

[a]*PIMM, ENSAM, CNRS, CNAM, 151 bd de l'Hôpital, 75013 Paris, France*
[b]*Airbus Safran Launchers, Centre de recherche du Bouchet, 9 rue Lavoisier, 91710 Vert-le-Petit, France*
[c]*LMS, Ecole Polytechnique, CNRS, Université Paris-Saclay, 91128 Palaiseau, France*

Abstract

The stress-strain response of a rubbery polymer network highly filled with micrometric glass beads was measured at low strain rate in uniaxial tension. The volume change of the glass bead filled material upon stretching was recorded by video extensometry and X-ray tomography scans were used to identify the type of damage within the composite material. The modeling used a cohesive-zone model from the literature depending on the polymer/glass adhesion energy that was measured by peeling polymer strips from a glass plate. Nonlinear finite element simulations were performed on representative three-dimensional microstructures defined by periodic cubic unit cells containing randomly dispersed spherical particles. Good reproductions of both the composite response and the volume change were obtained prior to the appearance of inner cracks.

Keywords: elastomers; glass beads; mechanical behavior; damage; cohesive zone

1. Introduction

Highly filled elastomers show significant volume changes upon uniaxial stretching (Lepie and Adicoff, 1975; Özüpek and Becker, 1997) due to substantial matrix debonding at the filler/rubber interface (Tao et al., 2013). In order to reproduce the stress-strain response of such materials, which

---

*Corresponding author. *Email address:* pierre.gilormini@ensam.eu

depends strongly on damage, one path has been to apply numerical simulation where cohesive zones describe interfacial debonding. Some studies accounting for the rubber hyperelasticity of the matrix material apply preferably to fiber-reinforced composites, with either a periodic (Zhong and Knauss, 1997, for instance) or random (Moraleda et al. 2009; Yang et al., 2012, among others) distribution of particles, or are related qualitatively to particle-reinforced elastomers (Toulemonde et al., 2016). Other studies handle three-dimensional random microstructures (Matouš et al. 2007, for instance, but for small applied strains only) which are more appropriate for elastomers filled with particles. In a recent contribution, Spring and Paulino (2015) run finite element simulations for a rubber matrix moderately filled with silica nanoparticles. While these authors provide an interesting study on the role of the bonded interphase displayed in such filled rubbers (as evidenced by Berriot et al., 2002, for instance), their account for damage at the rubber/silica interface via a cohesive zone model, involving debonding and therefore volume change, is questionable. These authors compared their model to data from the literature that are lacking evidence of volume change upon stretching: Yatsuyanagi et al. (2002) do not mention any volume change, while Suzuki et al. (2005) assume matrix debonding at the particles interface based on Gent and Park (1984) observations made on micrometric but not nanometric particles. While, as reported by Spring and Paulino (2015), debonding is evident when particles are of the size of micrometers, it is not clear that rubbers filled with silica nanoparticles experience significant volume changes, especially at strains limited to 35%. Starkova and Aniskevich (2010), for instance, reported against for a similar silica/rubber system. Therefore, it appears that the cohesive-zone model has not been confronted yet with adequate applications where both stress and volume variations with respect to applied strain are compared to experiments. Very recently, Ilseng et al. (2017) measured the stress-strain response and significant volume changes at quite large strains in two elastomers, and they did observe particle/matrix debonding directly with scanning electron microscopy, but extremely low volume fractions of micrometric ZnO particles (about 1%) were considered. Moreover, their very simplified finite element simulations used an axisymmetric cell containing a single spherical inclusion, and were limited to qualitative comparison.

In the current contribution, specimens of a rubbery polymer network filled with 55% of 250 μm glass beads were submitted to uniaxial tension while recording their volume changes. The composite material was manufactured in lab and several experimental tests were conducted in order to limit the number of unknowns among the parameters needed to run realistic

simulations, accounting for the behavior of the matrix and the filler/rubber debonding. Three-dimensional nonlinear finite element simulations were run on representative random microstructures and included the recent, thermodynamically consistent, cohesive-zone model of Spring et al. (2016). This reformulation of the original model of Park et al. (2009) prevents some issues that appear when a linear unloading/reloading relationship is applied, as shown by Spring et al. (2016) and by Gilormini and Diani (2017). Therefore, the results presented here provide a quantitative comparison of the mechanical behavior and damage evolution between a numerical model and an actual rubber matrix highly filled with micrometric particles.

This paper is organized as follows. First, the material preparation and characterization are described, including the two techniques used to measure volume changes and the peel test used to access adhesion energy. Then, the cohesive-zone model considered is briefly recalled and the finite element model is detailed. Finally, the stress-strain responses and the volume changes given by the simulations are compared with the experimental results.

2. Material characterization

2.1. Matrix material

The polymer matrix is an acrylate network obtained by the copolymerization of 98.8 mol% of methylacrylate (MA) and 1.2 mol% of poly(ethylene clycol) dimethacrylate (PEGDMA) of molar weight 750 g/mol used as crosslinking agent; 2,2-dimethoxy-2phenylacetophenone (DMPA) was added as photo-initiator. The mix was cured in a UVP ultraviolet chamber CL-1000 during 55 min. The peak of loss modulus was measured at 8°C during a temperature sweep dynamic mechanical test run at 1 Hz, and therefore the material stress-strain response at room temperature can be assumed independent of the strain rate if the latter is moderate. The acrylate uniaxial stress-strain response measured on standard H3 dogbone samples with 1.5 mm thickness at room temperature and at a low crosshead speed of 1 mm/min is shown in Figure 1, which corresponds to a strain rate of the order of 10^{-3} s^{-1}. An isotropic incompressible hyperelastic behavior with a strain energy given by

$$U = \frac{2G}{\gamma^2}(\lambda_1^\gamma + \lambda_2^\gamma + \lambda_3^\gamma - 3) \tag{1}$$

which is a simplified version of the general law of Ogden (1982), with the λ_i denoting the principal stretches ($\lambda_1\lambda_2\lambda_3 = 1$), could be fitted very accurately
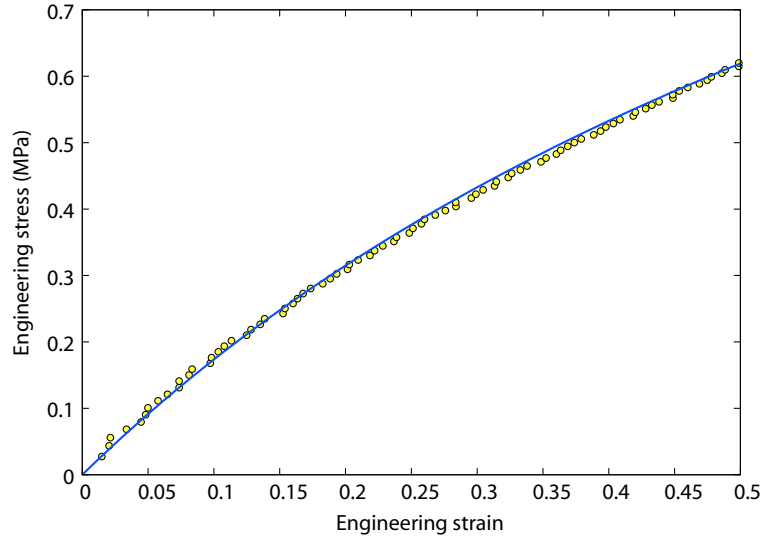
Figure 1: Experimental stress-strain response of the acrylate matrix in uniaxial tension (symbols) and comparison with the fitted incompressible hyperelastic law (solid line).

to these data. An initial shear modulus G of 0.637 MPa and an exponent $\gamma = 1.377$ lead to the curve shown in Figure 1. The incompressibility of the matrix material has been verified by applying the same video extensometry technique as described below in Section 2.3.

2.2. Filled composite

Following Cras et al. (1999), glass beads with an average diameter of 250 μm were immersed for 30 min in a 1:1 hydrochloric acid/ethanol mix, rinsed with distilled water and then dried during four hours in a hood. A 2/3 mass ratio of beads was added gradually to the polymer mix in order to avoid bead clustering. Then, the beads/polymer paste was poured between two glass plates which were maintained vertical during the curing in order to obtain a very highly filled polymer at the bottom. An anti-adhesive had been sprayed on the plates preliminarily to promote demoulding. The tomography observations reported in Section 2.3 below confirm that the material is free from bubbles at the end of this process, and densimetry measurements (with a precision of about $\pm$ 1%) showed that the final composite contains a 55% volume fraction of glass beads. Such a high volume fraction of particles was used because the composite was developed initially as a model for solid propellant-like materials.
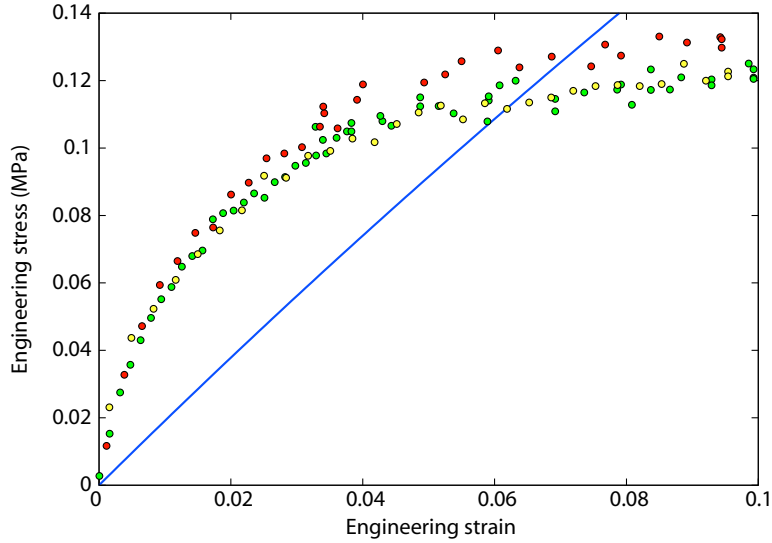
4

Figure 2: Experimental uniaxial stress-strain response of the composite material with 55% of glass beads (symbols, 3 tests). The fitted response of the acrylate matrix has been included for comparison (solid line).

The composite was loaded in uniaxial tension at 1 mm/min, and the results of 3 tests are reported in Figure 2. For small strains, the composite is clearly stiffer than the matrix, which reflects the expected effect of rigid reinforcements in a soft matrix. When strain proceeds, the tangent stiffness of the composite decreases significantly, due to the development of damage shown in Section 2.3 below. Finally, the softening effect of damage compensates the stiffening effect of reinforcements, and the response of the composite continues below that of the acrylate matrix, with a much smaller tangent stiffness. The slightly rough sides of the dogbone samples punched in a composite plate that contains a large volume fraction of glass beads are a likely cause of the data dispersion in Figure 2. In the next section, we show how damage evolves by measuring and observing void formation upon stretching.

2.3. Damage

Two damage mechanisms have been commonly observed when elastomers highly filled with micrometric particles are submitted to mechanical loadings: matrix/filler debonding (Oberth and Bruenner, 1965; Cornwell and Schapery, 1975; Tao et al., 2013) and crack appearance within the matrix

5

(Cornwell and Schapery, 1975; Ide and Ho, 1999). Both mechanisms generate voids and the evolution of damage upon loading can be linked directly to the macroscopic volume change since the rubber matrix is incompressible and the elastic glass beads do not deform at the stress levels considered (this has been checked in the simulations of Section 3.2). In the present study, two complementary techniques were used to quantify the amount of void created and to identify the type of damage occurring upon stretching: video extensometry and X-ray tomography.

Video extensometry measurements were carried out by merely painting four dots on two orthogonal stress-free faces of the central part of the standard H3 dogbone samples with 4 mm thickness. This procedure provides the volume change directly from the product of the measured principal stretches, without any assumption regarding isotropy for instance. Actually, the two cameras measured very similar transverse strains. On each face, two dots were aligned with the direction of stretching and two with the transverse direction. The principal stretches were extracted by postprocessing the images recorded by conventional cameras using a Matlab (2011) routine that we developed and which accounts for possible misalignments of the dots with respect to the principal directions of stretching. In addition, dogbone samples were submitted to tensile tests up to either 0.05 or 0.1 strain, and they were exposed to X-ray tomography while maintaining these strain values. The source parameters were 73 kV and 70 μA, resulting in a spatial resolution of 5 μm/pixel. The size of the post-treated volumes were at least $1000 \times 500 \times 400$ pixel^3 in order to comply with volume independence of the results. The matrix and the glass beads being incompressible and the volume fraction of beads being constant, it was possible to extract the void volume with a mere analysis of image gray levels by adapting the method of Bruchon et al. (2013), where a peak is chosen for each phase in the gray level histogram rather than threshold values. The main source of error in this procedure, leading to the error bar in Figure 3, is the precision of the required preliminary evaluation of the volume fraction of beads by densimetry.

Figure 3 displays the experimental volume variations obtained for an increasing applied strain. The volume changes very early and increases constantly. The tomography image of Figure 4a shows that no void is present in the unstrained sample, whereas matrix debonding has occurred around the particles throughout the microstructure after a macroscopic strain of 5% has been applied (Figure 4b). Due to a too low void volume leading to a hardly discernible peak of gray level, it was not possible to obtain a reliable value by X-ray tomography for the 5% strained specimen, but the
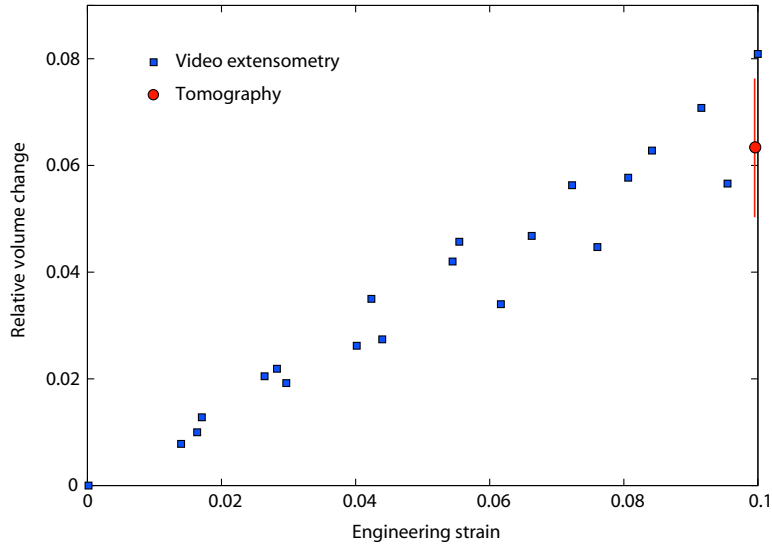
Figure 3: Relative volume changes upon uniaxial tension measured by video extensometry (3 tests) and by X-ray tomography (at 0.1 strain).

two techniques for measuring volume changes are in very good agreement at 10% strain (see Figure 3), where void growth is evident (Figure 4c). Moreover, some coalescence between voids can also be observed at 10% strain, which led to cracks in the composite. It may be noted that these observations are made in the volume of the material, and not merely at its free surface like in the works of Tao et al. (2013) and Ilseng et al. (2017). A given tomographic slice intersects beads at various distances from their centers, hence a large dispersion of the apparent size of bead sections.

2.4. Adhesion

In the modeling section, we intend to account for the observed matrix debonding at the filler interface, and therefore the adhesion properties of the polymer on glass must be evaluated. The studied composite is made of spherical glass beads embedded in the rubbery acrylate matrix, and it is assumed that the matrix/beads adhesion is similar to the adhesion between the matrix and a glass plate, provided that both the glass fillers and the glass plate have analogous chemical compositions and were submitted to the same surface preparation. Mixed-mode fracture occurs when the elastomer matrix debonds from a filler particle in the composite. However, an accurate characterization of the differences between the tangential and normal adhesions is very difficult (no mixed-mode bending test can be applied,
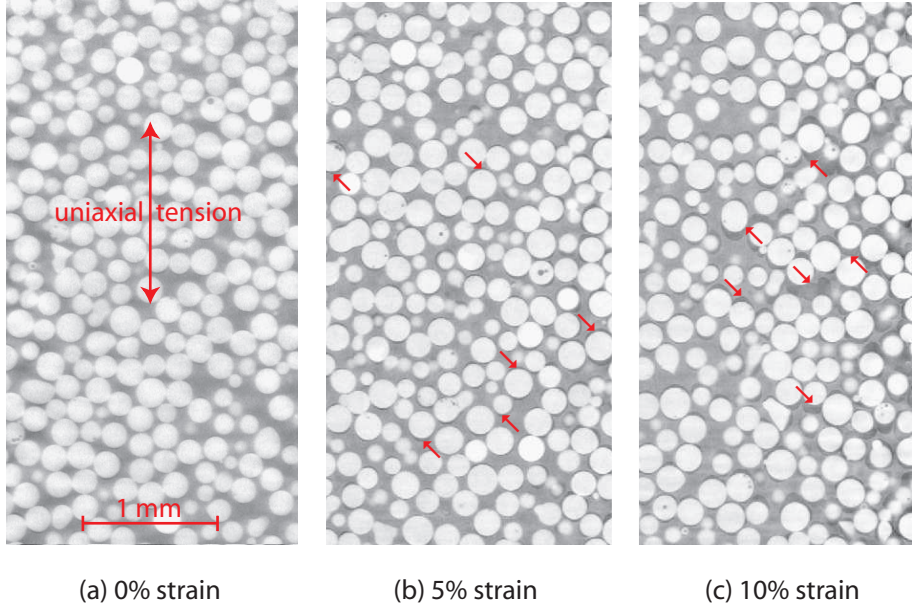
7

Figure 4: Typical tomographic slices through the volumes of the unstrained and strained samples, where voids appear in black. Examples of debonding (at 5% strain), cavity growth and coalescence (at 10% strain) are shown with arrows.

for instance), and the adhesion energy is assumed here independent of the fracture mode.

Glass plates were cleaned like the glass beads, and $110 \times 20 \times 0.3$ mm^3 strips of the acrylate matrix were cast and crosslinked on the treated glass plates. Following Gent and Petrich (1969), a woven cloth was glued on the back of the elastomer strip in order to make it inextensible. The peel test was conducted on a free-rolling bench at a velocity of 0.1 mm/s and a peel angle of 90°. The low peel rate used limits a viscous dissipation that may be due to a possibly viscoelastic behavior of the matrix and favors the assumption of an elastic behavior. Figure 5 presents the force recorded during a peel test. After the acrylate strip is put under tension, a steady peel process is established and the force stabilizes at 0.7±0.05 N. In these conditions, the peel separation work per unit area Γ can be related to the measured steady peel force F and to the width b of the inextensible peeled strip as $\Gamma = F/b$ (Rivlin, 1944; Lindley, 1971). It is very likely that some mode mixity develops in the process zone of the peel test, which is not known a priori, but the above assumption of mode independence allows to equate Γ
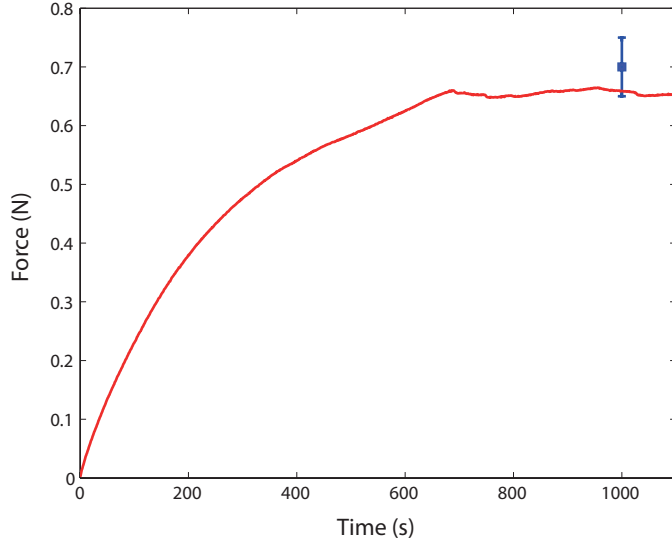
Figure 5: Force recorded during a peel test. The mean value and standard deviation of the stabilized force over 5 tests are also shown.

and the mode-independent elastomer/glass adhesion energy ϕ. This leads to an adhesion energy of 35 ± 3 J/m^2 that is consistent with results available in the literature (Ahagon and Gent, 1975).

3. Modeling

3.1. Cohesive-zone model

Consider a separation vector $\overrightarrow{\Delta}$ in a cohesive zone, with a normal component $\Delta_{\mathrm{n}} = \overrightarrow{\Delta}.\overrightarrow{n}$ and a tangential component $\Delta_{\mathrm{t}} = \sqrt{\overrightarrow{\Delta}.\overrightarrow{\Delta} - \Delta_{\mathrm{n}}^2}$. The case of negative Δ_{n} values, for which an elastic response applies, is not considered here to keep things simple, and therefore Δ_{n} is assumed positive in what follows. The reformulation by Spring et al. (2016) of the original model of Park et al. (2009) can be stated simply from the following dimensionless functions

$$\varphi_{\mathrm{n}}(\Delta_{\mathrm{n}}) = \left(\frac{\alpha}{m}\right)^m \left(1 - \frac{\Delta_{\mathrm{n}}}{\delta_{\mathrm{n}}}\right)^\alpha \left(\frac{m}{\alpha} + \frac{\Delta_{\mathrm{n}}}{\delta_{\mathrm{n}}}\right)^m$$

$$\text{and} \quad \varphi_{\mathrm{t}}(\Delta_{\mathrm{t}}) = \left(\frac{\beta}{n}\right)^n \left(1 - \frac{\Delta_{\mathrm{t}}}{\delta_{\mathrm{t}}}\right)^\beta \left(\frac{n}{\beta} + \frac{\Delta_{\mathrm{t}}}{\delta_{\mathrm{t}}}\right)^n \quad (2)$$

9

when both mode I and mode II fracture energies are equal, as assumed here. These functions are such that their product, changed signed, times the adhesion energy ϕ defines a potential whose first derivatives with respect to Δ_n and Δ_t give the normal (T_n) and tangential (T_t) traction components for continuous loading, respectively. In addition to ϕ, six material parameters are involved in the model: the normal and tangential cohesive strengths ($\sigma_{\max}$ and $\tau_{\max}$), the shape exponents $\alpha \geq 1$ and $\beta \geq 1$, and the ratios λ_n and λ_t between 0 and 1. The following quantities can be deduced from these parameters, which are used in (2):

$$m = \frac{\alpha(\alpha-1)\lambda_n^2}{1 - \alpha\lambda_n^2} \qquad \text{and} \qquad n = \frac{\beta(\beta-1)\lambda_t^2}{1 - \beta\lambda_t^2} \qquad (3)$$

as well as the normal (δ_n) and tangential (δ_t) separation lengths for mode I and mode II fractures, respectively:

$$\delta_n = \frac{\phi\,\alpha\,\lambda_n}{\sigma_{\max}}(1 - \lambda_n)^{\alpha-1}\left(1 + \frac{\alpha}{m}\right)\left(1 + \lambda_n\frac{\alpha}{m}\right)^{m-1} \quad \text{and}$$

$$\delta_t = \frac{\phi\,\beta\,\lambda_t}{\tau_{\max}}(1 - \lambda_t)^{\beta-1}\left(1 + \frac{\beta}{n}\right)\left(1 + \lambda_t\frac{\beta}{n}\right)^{n-1}. \quad (4)$$

With $\varphi_n'(\Delta_n)$ and $\varphi_t'(\Delta_t)$ denoting the first derivatives of $\varphi_n(\Delta_n)$ and $\varphi_t(\Delta_t)$, respectively, and with $\Delta_n^{\max}$ and $\Delta_t^{\max}$ being two state variables defined as the largest values of Δ_n and Δ_t reached so far, the normal and tangent traction components write as follows:

$$T_n = -\phi\,\varphi_n'(\Delta_n^{\max})\,\varphi_t(\Delta_t^{\max})\frac{\Delta_n}{\Delta_n^{\max}}$$

$$\text{and} \quad T_t = -\phi\,\varphi_t'(\Delta_t^{\max})\,\varphi_n(\Delta_n^{\max})\frac{\Delta_t}{\Delta_t^{\max}} \quad (5)$$

provided that no fracture has occurred yet, where the ratio $\Delta_n/\Delta_n^{\max}$ (resp. $\Delta_t/\Delta_t^{\max}$) should be omitted as long as $\Delta_n^{\max} = 0$ (resp. $\Delta_t^{\max} = 0$). Fracture occurs when either $\Delta_n = \delta_n$ or $\Delta_t = \delta_t$, which corresponds to T_n and T_t reaching zero values simultaneously for a non-zero separation. For a purely normal (resp. tangential) and continuously increasing separation, this confirms the physical interpretation of δ_n (resp. δ_t) as the separation length for mode I (resp. mode II) fracture. When fracture has occurred, T_n and T_t keep zero values during further loading history. It can be checked by integration of (5) that ϕ is the energy that is dissipated up to fracture along any loading path where Δ_n and Δ_t never decrease. This applies especially,
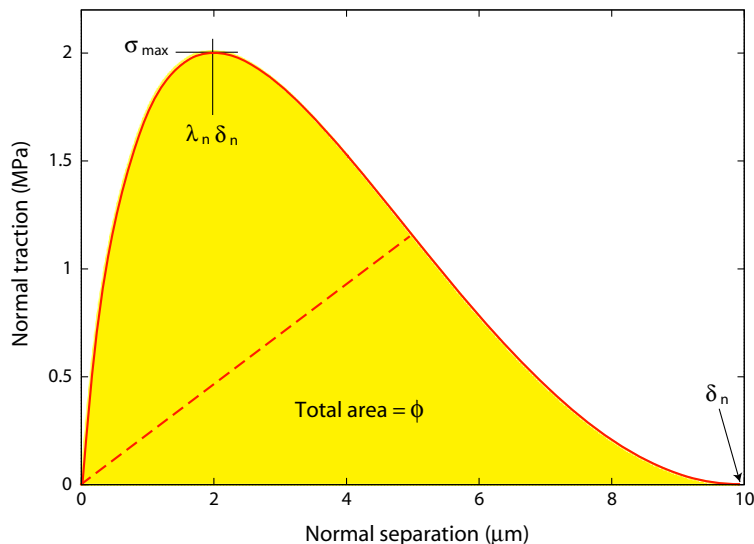
Figure 6: Example of the normal traction T_n induced in the cohesive zone when mode I separation Δ_n increases continuously (solid line) or during unloading/reloading after a separation of 5 μm has been applied (dashed line). The following parameter values were used: $\phi = 10$ J/m^2, $\sigma_{max} = 2$ MPa, $\alpha = 3$ and $\lambda_n = 0.2$, hence $\delta_n = 9.9$ μm.

but not only, to proportional loadings, and makes the evaluation of ϕ from the peel test described in Section 2.4 quite plausible.

It can be checked easily that unloading and reloading, defined by $\Delta_n < \Delta_n^{max}$ and $\Delta_t < \Delta_t^{max}$, perform linearly to the origin according to (5). This is true not only for pure mode I (as illustrated in Figure 6) or mode II, but for any mixed mode. As shown recently by Spring et al. (2016) and by Gilormini and Diani (2017), this contrasts with what is obtained when the original cohesive-zone model of Park et al. (2009) is combined with a linear unloading/reloading relationship like in the numerical implementation given by Spring and Paulino (2014) for 3D finite element simulations.

3.2. Finite element modeling

Computing time is a major concern when nonlinear finite element simulations are performed on three-dimensional microstructures, because of the number of particles to consider, the number of elements required, the number of successive load increments, and the number of iterations per increment. A typical simulation described below for an applied engineering strain of

0.10, involving both finite strain and material nonlinearities, lasted about 22 h when using 4 nodes of a cluster computer where each node consists of two 6-core processors. Because of the number of simulations required by this study, which included some parameter fitting, this is the upper limit that we could afford. This corresponds to using about 270,000 elements with a total of about 1,300,000 unknowns. One computation has been run with a doubled number of elements and unknowns, which multiplied the computing time by more than 7 with no significant change noticed in the results. With the number of elements given, a good compromise for the number of spherical particles to consider was found at about 50, which is comparable to what is used in other studies on similar topics and corresponds to an average of about 4,700 solid elements (and 700 cohesive elements) per particle, including both the particle itself and the surrounding matrix.

The finite element simulations used a unit cell to which periodic boundary conditions were applied. The cubic unit cell contained 54 identical spheres that were initially distributed on a body-centered cubic (BCC) lattice and were moved randomly according to a three-dimensional adaptation of the two-dimensional algorithm MCDISKS of Torquato (2002). More precisely, three million iterations were applied after a random number generator had been initialized to a value that could be changed in order to get different final distributions of the spheres in the cell. Large numbers of iterations are required at high volume fractions because of the small space left between the spheres, so that each random displacement is restrained severely. Figure 7 shows an example of a unit cell that has been generated by this procedure, where periodicity of the microstructure has been obtained by suitably replicating any sphere that intercepted the limits of the cell. In the case of Figure 7, this resulted in a total of 115 complete or partial spheres in the cubic cell (Figure 7b). The spheres diameter was 250 μm and the sides of the cubic cell were 930 μm long, which corresponds to an inclusion volume fraction of 55%. In order to avoid mesh distortion induced by too small matrix bridges between particles, which are not excluded by the applied random displacements, the volume fraction used when generating the microstructure was 56%, and all spheres were subsequently shrunk by the same amount to reach the volume fraction of 55%. This guaranteed that the surfaces of any pair of particles were at least 1.6 μm apart, which corresponds to 0.6% of the sphere diameter. This is a reasonable compromise according to the systematic study of Gusev (2016) in small strain elasticity, where this value leads to the shear modulus of a composite with 55% of SiO_2 spheres in a rubber matrix being 8.5% lower than the limit for allowed contact between spheres.
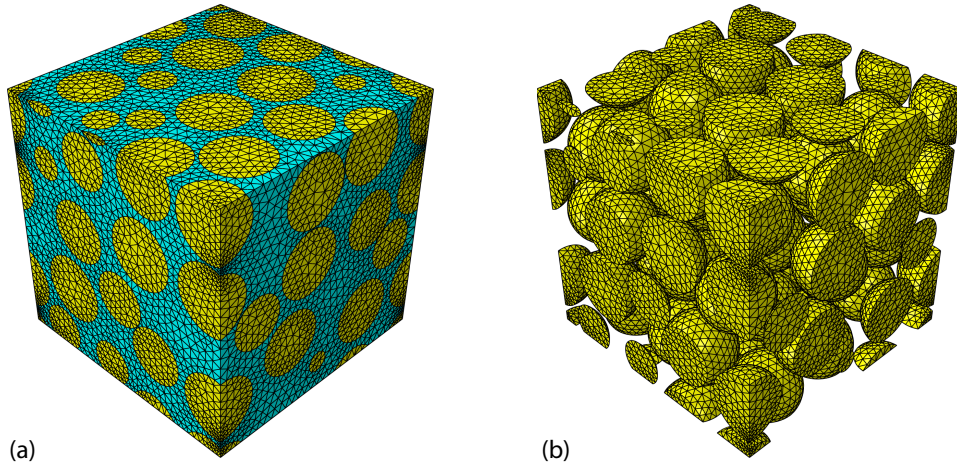
12

Figure 7: An example of a periodic unit cell used to simulate a random distribution of spheres (55% volume fraction) in a matrix. Mesh of the unit cell (a) and detail of the mesh of the inclusions only (b).

Using a periodic cell also requires adequate boundary conditions to ensure that the displacements on opposite cell faces differ by the same values, so that a unit cell remains perfectly bonded to all its neighbor, identical, cells. This also requires that the meshes of opposite faces are the same, so that each node has an exact opposite. These two requirements could be managed easily by generating the mesh of the unit cell with Netgen (Schöberl, 1997), which provided both a periodic mesh and the set of linear constraints between node displacements that could be used directly with the Abaqus (2012) finite element code. In the example of Figure 7, the mesh involved 102,433 elements in the elastomeric matrix and 135,427 elements in the inclusions. All elements were 10-node quadratic tetrahedra with full integration, using a hybrid formulation in the elastomeric phase (i.e., using both the displacements and the pressure as unknowns) because of the incompressible behavior considered, whereas a usual displacement formulation was employed in the glass inclusions, where a Young's modulus of 69 GPa and a Poisson's ratio of 0.25 were used. In addition, cohesive elements with an initial zero thickness have been inserted at the interfaces between the inclusions and the matrix phase. Each 6-node triangular face shared by one tetrahedral element in the inclusion and one tetrahedral element in the matrix has been duplicated in order to define a 12-node cohesive element. Therefore, additional nodes and additional constraints for periodicity

13

conditions had to be introduced. In the example of Figure 7, this process generated 36,252 cohesive elements, leading to a total of 505,080 nodes and 1,315,498 unknowns. Similar values have been obtained with the two other microstructures that had been generated by varying the initialization of the random process.

It must be mentioned that using the cohesive interface or the cohesive elements available in Abaqus has been rejected in this study. First, the cohesive interface was found questionable by Gilormini and Diani (2015) in their analysis of various implementations of a cohesive-zone model in plane strain. Yet, this would have allowed representing the spherical particles as rigid bodies (the strain in the inclusions is found 4 orders of magnitude smaller than the applied strain in the simulations below), thus meshing the matrix phase only. Since the Netgen mesh generator uses tetrahedral elements only and does not include rigid solids, using the Abaqus cohesive elements has been rejected too because only 6-node elements were available that required using 4-node tetrahedra as solid elements. In the simple case of a periodic distribution of spheres, the latter solid elements required a very fine mesh with a number of unknowns that would be prohibitive for random microstructures to get the same precision as with 10-node tetrahedra. In addition, Park et al. (2016) have shown recently that the traction-separation relationship used in the cohesive elements of Abaqus can lead to non-physical responses. Therefore, a 12-node user-defined cohesive element was used here, which provided smooth convergence in all cases considered. This element has been presented by Spring and Paulino (2014) and is available from the website of the latter author. In its original form, this element uses the cohesive-zone model of Park et al. (2009) that we replaced by the thermodynamically consistent model of Spring et al. (2016). The expression of the tangent matrix given in the latter paper was used.

After the mesh has been defined, uniaxial tension could be applied along any of the coordinate axes by prescribing the displacement of a node located at a corner of the cubic cell and by applying the standard periodic boundary conditions defined by Segurado and Llorca (2002), for instance, which are used in all similar studies. In these conditions, the nodes on the faces of the unit cell parallel to the tensile axis are allowed to translate so that the corresponding total force on each face is zero and periodicity is ensured.

As explained above, 54 spherical particles seemed a good compromise between the number of elements allowed and the representativity of the unit cell. We note first this leads to a ratio of 3.72 for the edge of the unit cell divided by a sphere diameter, which is close to the value of 3.74 obtained by Segurado and Llorca (2002) for a representative volume element in small

strain elasticity, in agreement with the analytical study of Drugan and Willis (1996). In addition, we note that the coordinates of the centroids of the three microstructures considered here are found very close to the center of the unit cell (to less than 0.3% of the cube edge length) when mass densities of 1 and 0 are assigned to the spheres and to the matrix phase, respectively. Moreover, the moments of inertia with respect to the three coordinate axes are within 1% or less of the corresponding value for a homogeneous cube of equivalent mass, which was suggested by Segurado and Llorca (2002) as a criterion for no preferential direction to exist in the unit cell. Unfortunately, such directions do exist if no random displacement is applied to the initial BCC network of spheres, and the moments of inertia are 0.18% close to the values for the homogeneous cube. Therefore, the moment of inertia is not a reliable criterion for the isotropy of the spheres distribution.

A more direct approach was used instead, where both phases were considered as incompressible and in small strain elasticity (whereas finite strains are considered in Section 4) with perfect adhesion (no cohesive elements added), i.e., the behaviors of the spheres and the matrix were defined by the shear modulus only (23 GPa and 0.6 MPa, respectively). In these conditions, a ratio of 3 between the Young's modulus and the shear modulus is expected for an isotropic composite, and an average value of 3.4 was obtained with the three microstructures (three loadings in uniaxial tension and three loadings in simple shear for each). This allows to appreciate the effect of the random displacements applied during the preparation of the microstructures, since simulations performed on a finely meshed minimal unit cell for a BCC network led to a ratio of 1.3, clearly far from isotropy. The average shear modulus obtained with the random microstructures is 6.13±0.44 MPa and the Young's modulus is 20.84±2.09 MPa, with a larger standard deviation consequently. The shear modulus is very close to the limit value of about 6.2 that can be deduced from the results of Gusev (2016) on a SiO_2/rubber system, where we notice similar standard deviations. The relatively approximate isotropy obtained here with random microstructures can be due to the large volume fraction of identical spheres: as noted by Rintoul and Torquato (1998), a system of identical spheres tends to order locally and to form crystallites above the volume fraction of 49.4%. As a consequence, the size of an isotropic representative volume element is likely to increase rapidly in order to average off the orientations of such crystallites, and it may exceed our computing capabilities. Nevertheless, we anticipate on the results obtained below, which show a mechanical response in uniaxial tension that is remarkably equal whatever the coordinate axis chosen and the microstructure considered when all nonlinearities are included.
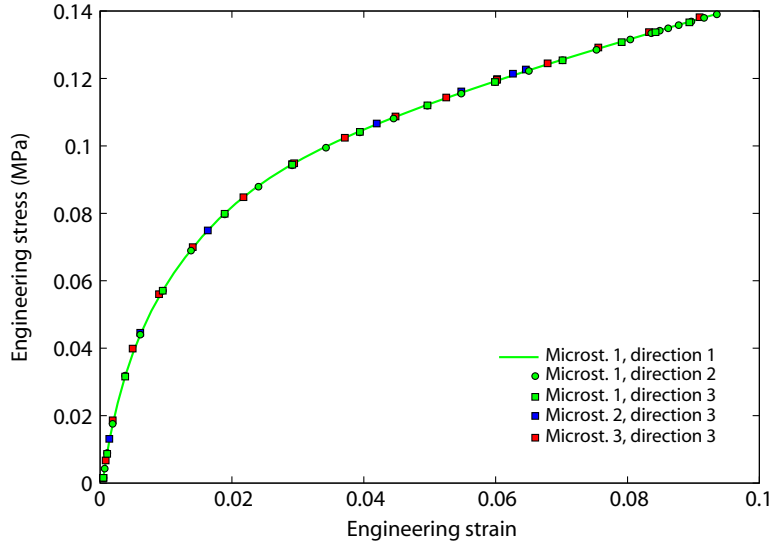
15

Figure 8: Comparison between finite element simulations when uniaxial tension is applied either along each coordinate axis of the microstructure shown in Figure 7 (green line, circular and square symbols) or along the same coordinate axis in two other random microstructures (blue and red square symbols). Symbols are used to sample the corresponding curves for easier comparisons.

4. Results

The effects of changing the tensile direction and the random microstructure considered in the finite element simulations is analyzed first. Figure 8 shows the results obtained in 5 cases, where uniaxial tension was applied along each coordinate axis in turn (3 cases) on the microstructure shown in Figure 7, or where uniaxial tension was applied along a given tensile axis on two additional random microstructures generated with the procedure described in the previous section (2 cases). The results are so close to each other that a sampling of the results has been used in four cases to allow comparison between curves that would not be distinguishable otherwise. This confirms the assessment made above that the microstructures considered, despite their relatively small number of particles and slight anisotropy for a linear behavior, are representative enough for the nonlinear behaviors considered in this study. The concordance of results in Figure 8 when three different microstructures are considered conveys also that no defect is present, in contrast to the rough lateral sides of the experimental samples mentioned in Section 2.2. A simulation was also run with a 0.54 volume
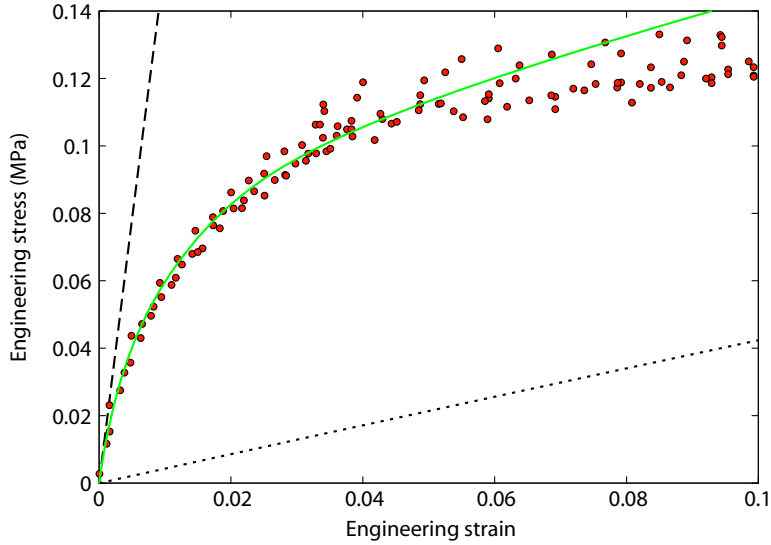
16

Figure 9: Comparison between the finite element model (solid line) and experimental data for the composite: stress-strain response in uniaxial tension. The perfect adhesion (dashed line) and no-adhesion (dotted line) cases are also shown.

fraction of fillers, in order to evaluate the effect of uncertainty on this parameter, and the results were found extremely close to (slightly below) the curve shown in Figure 8.

In addition to a Young's modulus of 69 GPa and a Poisson's ratio of 0.25 for the glass beads, an initial shear modulus G of 0.637 MPa and an exponent $\gamma = 1.377$ for the acrylate matrix, the simulations shown in Figure 8 used the following set of parameters for the cohesive-zone model: $\phi = 35$ J/m^2, $\sigma_{\max} = 45$ kPa, $\tau_{\max} = 70$ kPa, $\alpha = \beta = 3$, $\lambda_{\mathrm{n}} = 9 \times 10^{-4}$ and $\lambda_{\mathrm{t}} = 6 \times 10^{-3}$, which are also the values used in Figures 9, 10 and 11. The ϕ value is the one obtained from the peel test, λ_{n} and λ_{t} have been tuned so that the initial slope of the stress-strain curve is very close to the case of a perfect adhesion (with no relative displacement allowed at the particles/matrix interfaces), while preserving convergence and reasonable computing time. We note in passing that the good agreement in Figure 9 between a perfect adhesion and the experimental results at very low strains is a further validation of the finite element simulations, which are representative of a polymer matrix reinforced by a 55% volume fraction of randomly dispersed spheres without damage. A very large space is left in Figure 9 between the responses induced by the two extreme interface behaviors, namely the case of a perfect adhesion and
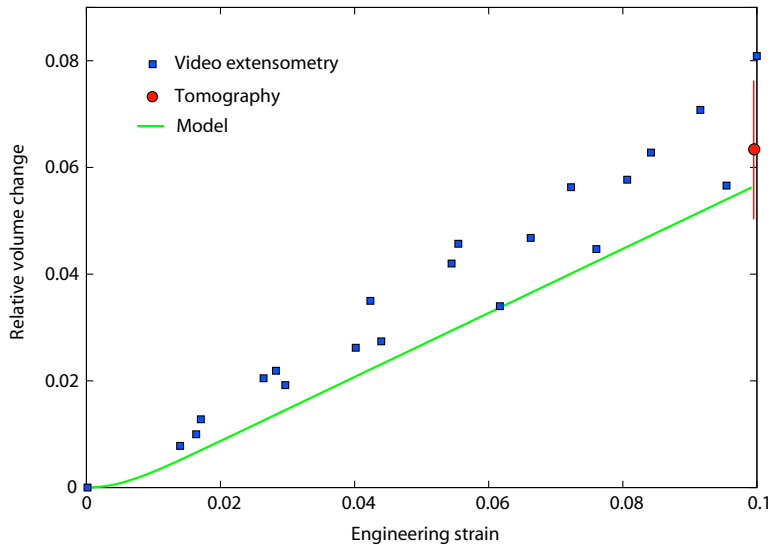
17

Figure 10: Comparison between the finite element model (solid line) and experimental data for the composite: relative volume change recorded during uniaxial tension.

the case of no adhesion at all (merely preventing interpenetration between the matrix and the particles, without friction). This large span can be covered by varying the parameters of the cohesive zone, and therefore a careful adjustment procedure is required. Among the four parameters left to determine, $\sigma_{\max}$ and $\tau_{\max}$ had the largest influence on the computed stress-strain response of the composite. They allowed to adjust the curvature of the response so as to reproduce well the experimental results, and taking $\sigma_{\max}$ different from $\tau_{\max}$ has been fruitful in this respect. The exponents α and β had a minor effect and it has not been found useful to give them different values.

As shown in Figure 9, the softening effect of a damaging interface is reproduced quite well up to an applied strain of about 0.06. Beyond this value, the stress predicted by the finite element simulation exceeds the experimental results, and the ongoing tangent stiffness, which is similar to what is obtained without adhesion, is too large. This may be due to the occurrence of void coalescence, which could be observed by tomography at 0.10 strain (Figure 4c) but not at 0.05 (Figure 4b), and which cannot be modeled without including a rupture of the matrix material that is beyond the simulations presented here.

Figure 10, which has not been used to fit any parameter, shows that
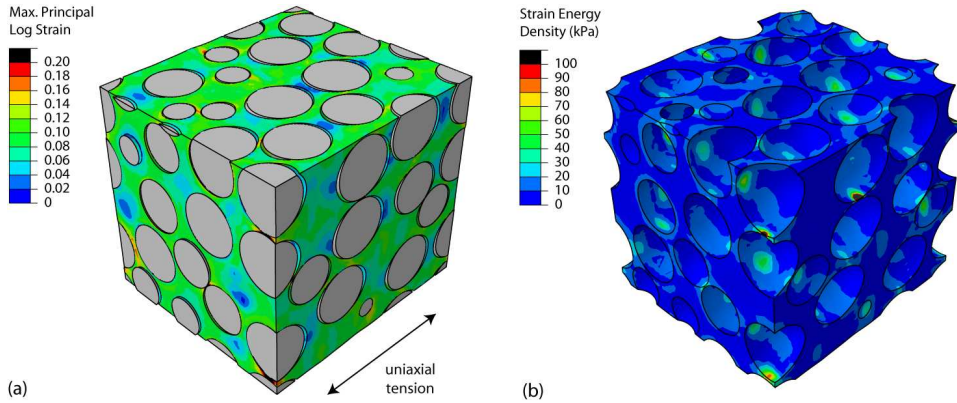
18

Figure 11: Maps of the maximal principal logarithmic strain (a) and of the density of elastic strain energy in the matrix (b) obtained after a uniaxial tension (10% elongation) has been applied to the microstructure shown in Figure 7.

the model slightly underestimates the experimental volume changes. This is consistent with an additional void volume that may be induced by defects along the sides of the dogbone samples. Noticeably, the agreement applies beyond the one found for the applied force, i.e., in the strain range where coalescence occurs and induces microcracks. This may result from a balance between two opposite effects: a direct increase of void volume due to the microcracks opening and an indirect decrease of void volume at debonded particles in the vicinity of microcracks because of the elastic strain relaxation that their appearance induces. The results of Figure 10 beyond a strain of 0.06 suggest that merely growing the voids at debonded particles without creating microcracks in the simulations leads to a void volume of the right order in the present case.

Figure 11a illustrates the void openings obtained after 10% elongation and can be compared with Figure 4c. Of course, no coalescence is observed in the simulations, where debonding is evident, but large strain hetero-geneities are located in interparticle bridges, especially where they are very thin. Consistently, the density of elastic strain energy in the matrix, which would be of 8.9 kPa if the material were 100% acrylate, is rather uniformly distributed except in particle bridges (Figure 11b), where more than ten times this value can be reached, suggesting that matrix rupture is likely to occur. This would be consistent with the coalescence of voids between very close particles.

In the literature, quantitative comparisons of experimental results and

finite element simulations of the stress-strain response of damaging reinforced elastomers are very scarce, although several numerical analyses can be found. The satisfactory stress-strain responses obtained by Spring and Paulino (2015) up to a large applied strain of 0.35 for a rubber matrix reinforced with 26% of silica particles have already been discussed in the Introduction in relation with no volume change being reported. In the different context of an elastic-plastic matrix (aluminum) reinforced by rigid particles (tungsten carbide) with damageable interfaces, Segurado (2004) compared finite element simulations using the formulation of Segurado and Lorca (2004) and experimental stress-strain curves. A bilinear cohesive-zone model was used with parameter values taken from the literature. The agreement is pretty good for a 10% volume fraction of particles up to an elongation of 0.06, but is less satisfactory for a 30% volume fraction at the very small strain reached before specimen rupture. A strong difference with the elastomeric matrix of the present study must be noted, however: the span between perfect adhesion and no adhesion is very narrow in the elastic-plastic case considered, which may favor an easier concordance between simulations and experiments.

5. Summary and concluding remarks

A composite material was prepared, where a polymer network in the rubbery state was filled with a large volume fraction of micrometric spherical glass beads. The composite stress-strain response in uniaxial tension was recorded at a low strain rate. Two techniques were combined to measure volume changes, including X-ray tomography analysis which allowed to assess that damage inside the composite develops as an early filler/rubber debonding followed by the growth and coalescence of voids. Several material parameters were determined: the hyperelastic behavior of the polymer network in uniaxial tension was characterized, the volume fraction of glass beads contained in the composite was measured, and the adhesion energy between the polymer and glass was obtained from a peel test.

For finite element simulations, three cubic cells containing 54 randomly dispersed spheres were created for finite element simulations, where periodic boundary conditions were prescribed. The incompressible polymer matrix behavior was accurately reproduced by a hyperelastic strain energy, the glass beads were elastic with standard glass moduli, and the debonding at the filler/rubber interface was described by using cohesive elements that applied a thermodynamically consistent cohesive-zone model.

The comparisons between the simulations and the experimental results showed that it was possible to replicate the composite stress-strain response up to void coalescence by adjusting the missing parameters of the cohesive-zone model. Once this was done, the volume changes were predicted quite well.

In order to further challenge the model, additional types of loadings might be applied to the composite specimens, such as biaxial tension or shearing. It would also be interesting to explore the impact of a change in the particles size, since a cohesive zone introduces a characteristic length. Finally, including a fracture criterion in the matrix material throughout the composite would probably allow the simulations to reproduce the experimental observations at larger applied strains.

Acknowledgments

References

Abaqus, 2012. Dassault Systèmes Simulia Corporation. Providence, RI, USA.

Ahagon, A., Gent, A.N., 1975. Effect of interfacial bonding on the strength adhesion. J. Polym. Sci. 13, 1619-1633.

Berriot, J., Montes, H., Lequeux, F., Long, D., Sotta, P., 2002. Evidence of the shift of the glass transition near the particles in silica-filled elastomers. Macromolecules 35, 97569762.

Bruchon, J.F., Pereira, J.M., Vandamme, M., Lenoir, N., Delage, P., Bornert, M., 2013. Full 3D investigation and charaterisation of capillary collapse of a loose unsaturated sand using X-ray CT. Granular Matter 15, 783-800.

Cornwell, L.R., Schapery, R.A., 1975. SEM study of microcracking in strained solid propellant. Metallography 8, 445-452.

Cras, J.J., Rowe-Taitt, C.A., Nivens, D.A., Ligler, F.S., 1999. Comparison of chemical cleaning methods of glass in preparation for silanization. Biosensors Bioelec. 14, 683-688.

Drugan, W.J., Willis, J.R., 1996. A micromechanics-based nonlocal constitutive equation and estimates of representative volume element size for elastic composites. J. Mech. Phys. Solids 44, 497-524.

Gent, A.N., Park, B., 1984. Failure processes in elastomers at or near a rigid spherical inclusion. J. Mater. Sci. 19, 1947-1956.

Gent, A.N., Petrich, R.P., 1969. Adhesion of viscoelastic materials to rigid substrates. Proc. Roy. Soc. London 310, 433-448.

Gilormini, P., Diani, J., 2015. Testing some implementations of a cohesive-zone model at finite strain. Engng. Fract. Mech. 148, 97-109.

Gilormini, P., Diani, J., 2017. Some features of the PPR cohesive-zone model combined with a linear unloading/reloading relationship. Engng. Fract. Mech. 173, 32-40.

Gusev, A.A., 2016. Controlled accuracy finite element estimates for the effective stiffness of composites with spherical inclusions. Int. J. Solids Struct. 80, 227-236.

Ide, K.M., Ho, S.Y., 1999. Fracture behaviour of accelerated aged solid rocket propellants. J. Mater. Sci. 34, 4209-4218.

Ilseng, A., Skallerud, B.H., Clausen, A.H., 2017. An experimental and numerical study on the volume change of particle-filled elastomers in various loading modes. Mech. Mater. 106, 44-57.

Lepie, A.H., Adicoff, A., 1975. Energy balances and uniaxial damage of highly filled elastomers. J. Appl. Polym. Sci. 19, 2821-2830.

Lindley, P.B., 1971. Ozone attack at a rubber-metal bond. J. Inst. Rubber Ind. 4, 1186-1195.

Matouš, K., Inglis, H.M., Gu, X., Rypl, D., Jackson, T.L., Geubelle, P.H., 2007. Multiscale modeling of solid propellants: From particle packing to failure. Compos. Sci. Technol. 67, 1694-1708.

Matlab, 2011. The MathWorks Inc. Natick, MA, USA.

Moraleda, J., Segurado, J., Llorca, J., 2009. Finite deformation of incompressible fiber-reinforced elastomers: A computational micromechanics approach. J. Mech. Phys. Solids 57, 1596-1613.

Oberth, A.E., Bruenner, R.S., 1965. Tear phenomena around solid inclusions in castable elastomers. Trans. Soc. Rheol. 9, 577-588.

Ogden, R.W., 1982. Elastic deformations of rubberlike solids. Mechanics of Solids, the Rodney Hill 60th Anniversary Volume, Eds. Hopkins H.G. and Sewell M.J., Pergamon, 499-537.

Özüpek, S., Becker, E.B., 1997 Constitutive equations for solid propellants. J. Engng. Mater. Technol. 119, 125-132.

Park, K., Choi, H., Paulino, G.H., 2016. Assessment of cohesive traction-separation relationships in ABAQUS: A comparative study. Mech. Res. Comm. 78, 71-78.

Park, K., Paulino, G.H., Roesler, J.R., 2009. A unified potential-based cohesive model of mixed-mode fracture. J. Mech. Phys. Solids 57, 891-908.

Rintoul, M.D., Torquato, S., 1998. Hard-sphere statistics along the metastable amorphous branch. Phys. Rev. E 58, 532-537.

Rivlin, R.S., 1944. The effective work of adhesion. Paint Technol. 9, 2611-2614.

Schöberl, J., 1997. NETGEN an advancing front 2D/3D-mesh generator based on abstract rules. Comput. Visual. Sci. 1, 41-52.

Segurado, J., 2004. Micromecánica computational de materiales compuestos reforzados con partículas. PhD thesis, Technical University of Madrid, Spain.

Segurado, J., Llorca, J., 2002. A numerical approximation to the elastic properties of sphere-reinforced composites. J. Mech. Phys. Solids 50, 2107-2121.

Segurado, J., Llorca, J., 2004. A new three-dimensional interface finite element to simulate fracture in composites. Int. J. Solids Struct. 41, 2977-2993.

Spring, D.W., Giraldo-Londoño, O., Paulino, G.H., 2016 A Study on the Thermodynamic Consistency of the Park-Paulino-Roesler (PPR) cohesive fracture model. Mech. Res. Comm. 78, 100-109.

23

Spring, D.W., Paulino, G.H., 2014. A growing library of three-dimensional cohesive elements for use in ABAQUS. Engng. Fract. Mech. 126, 190-216.

Spring, D.W., Paulino, G.H., 2015. Computational homogenization of the debonding of particle reinforced composites; the role of interphases in interfaces. Comput. Mater. Sci. 109, 209-224.

Starkova, O., Aniskevich, A., 2010. Poisson's ratio and the incompressibility relation for various strain measures with the example of a silica-filled SBR rubber in uniaxial tension tests. Polym. Testing 29, 310-318.

Suzuki, N., Ito, M., Yatsuyanagi, F., 2005 Effects of rubber/filler interactions on deformation behavior of silica filled SBR systems. Polymer 46, 193-201.

Tao, Z.J., Ping, S.D., Mei, Z., Cheng, Z.P., 2013. Microstructure deformation and fracture mechanism of highly filled polymer composites under large tensile deformation. J. Phys. Conf. Ser. 419, 12014-12020.

Torquato, S., 2002. Random Heterogeneous Materials – Microstructure and Macroscopic Properties. Springer-Verlag Inc., New York.

Toulemonde, P.A., Diani, J., Gilormini, P., 2016. On the account of a cohesive interface for modeling the behavior until break of highly filled elastomers. Mech. Mater. 93, 124-133.

Yang, L., Yan, Y., Liu, Y., Ran, Z., 2012. Microscopic failure mechanisms of fiber-reinforced polymer composites under transverse tension and compression. Compos. Sci. Technol. 72, 1818-1825.

Yatsuyanagi, F., Suzuki, N., Ito, M., Kaidou, H., 2002. Effects of surface chemistry of silica particles on the mechanical properties of silica filled styrene-butadiene rubber systems. Polym. J. 34, 332-339.

Zhong, X.A., Knauss, W.G., 1997. Analysis of interfacial failure in particle-filled elastomers. J. Engng. Mater. Technol. 119, 198-204.